Decoration of Ag Species into Reduced Graphene Oxide Foam as a Superelastic and Robust Host toward Stable Zn Metal Anodes under Dwell-Fatigue Condition

Zheng, Ya Qi; Sun, Peng Xiao; Zhang, Xin Yu; Li, Nian Wu; Wu, Lili; Luan, Deyan; Zhang, Xitian; Lou, Xiong Wen (David); Yu, Le

Published in:
Advanced Materials

Published: 15/08/2024

Document Version:
Final Published version, also known as Publisher's PDF, Publisher's Final version or Version of Record

Published version (DOI):
10.1002/adma.202405906

Publication details:
Zheng, Y. Q., Sun, P. X., Zhang, X. Y., Li, N. W., Wu, L., Luan, D., Zhang, X., Lou, X. W., & Yu, L. (2024). Decoration of Ag Species into Reduced Graphene Oxide Foam as a Superelastic and Robust Host toward Stable Zn Metal Anodes under Dwell-Fatigue Condition. *Advanced Materials*, *36*(33), Article 2405906. https://doi.org/10.1002/adma.202405906

ADVANCED MATERIALS
www.advmat.de

Decoration of Ag Species into Reduced Graphene Oxide Foam as a Superelastic and Robust Host toward Stable Zn Metal Anodes under Dwell-Fatigue Condition

Ya Qi Zheng, Peng Xiao Sun, Xin Yu Zhang, Nian Wu Li, Lili Wu, Deyan Luan, Xitian Zhang, Xiong Wen (David) Lou, and Le Yu**

Deep-sea equipment usually operates under dwell-fatigue condition, which means the equipped energy storage devices must survive under the changing pressure. Special mechanical designs should be considered to maintain the electrochemical performance of electrodes under this extreme condition. In this work, an effective assembly strategy is proposed to accommodate the dwell-fatigue loading using Ag decorated reduced graphene oxide (rGO) foam (denoted as AGF) as a superelastic and robust Zn host. The wet-press assembly process enables the formation of highly porous and robust framework. The strong synergetic effect between rGO and Ag further guarantees AGF's superelasticity and ultrahigh mechanical strength. Meanwhile, the homogeneously distributed Ag species on the rGO sheets act as zincophilic sites to effectively facilitate Zn plating. Furthermore, AGF offers enough space to address the expansion during the charge and discharge cycles. As expected, the symmetrical cell using this AGF@Zn host demonstrates a long lifespan over 400 h at a depth-of-discharge of 50%. It is worth mentioning that the superelastic AGF host realizes stable Zn plating/stripping under varying pressures.

1. Introduction

With accelerating demand for the modern society, the application scenarios for energy storage devices are greatly broadened, therefore the necessity for reliable safe batteries in harsh environments is largely required.[1–4] Especially, deep-sea exploration encounters complex marine environment and uncertain equipment operation, where the influence of random loads must be considered for the affiliated battery system. Apart from the safety concerns, dwell-fatigue and high-pressure conditions in deep sea bring significant challenges to both materials and structures of the electrodes.[5–7] Usually, cell capacity is largely reduced and electrodes are prone to be pulverized under high hydrostatic pressure.[8]

Rechargeable Zn-ion batteries (ZIBs) present remarkable superiority over traditional lithium-ion batteries in confined space of underwater vehicles, where aqueous electrolyte is intrinsically safe. Among available ZIB anodes, metallic Zn is considered the optimal choice in view of its high theoretical capacity of 5854 mAh cm^{-3}, low reduction potential and abundant reserves.[9–15] Nevertheless, Zn metal anodes (ZMAs) still suffer from severe dendrite growth, side reactions such as hydrogen evolution reaction (HER) and self-corrosion reaction.[16–23] Moreover, ZMAs must function well in the variational pressure condition to meet the requirement of ZIBs in deep-sea equipment. Thus, special designs are needed to realize dendrite-free Zn deposition and enhance fatigue-resistance under extreme conditions.

Utilization of three-dimensional (3D) hosts has been recognized as an effective approach for ZMA by alleviating dendrite growth and buffering volume expansion during Zn plating/stripping.[10,17] Specially, graphene-based materials are considered as suitable host choices owing to their lightweight and high electrical conductivity.[13,24] As a typical representative, reduced graphene oxide (rGO) is a promising component to

Y. Q. Zheng, P. X. Sun, X. Y. Zhang, N. W. Li, L. Yu
State Key Lab of Organic–Inorganic Composites
Beijing University of Chemical Technology
Beijing 100029, P. R. China
E-mail: yule@mail.buct.edu.cn
The ORCID identification number(s) for the author(s) of this article can be found under https://doi.org/10.1002/adma.202405906

DOI: 10.1002/adma.202405906

L. Wu, X. Zhang
School of Physics and Electronic Engineering
Harbin Normal University
Harbin 150025, P. R. China
D. Luan, X. W. (David) Lou
Department of Chemistry
City University of Hong Kong
83 Tat Chee Avenue, Kowloon, Hong Kong 999077, P. R. China
E-mail: david.lou@cityu.edu.hk

build robust and superelastic micro-nanostructures because of its outstanding strength, elasticity, and strong interfacial interactions between various materials.[7,25–27] For example, the silicate-bridged graphene assembly with polygonal nanopores interconnected by silicon–oxygen chemical bonds exhibits an extremely high hardness of 13.09 GPa.[25] In another case, the wet-press assembled graphene aerogel possesses outstanding compressive strength (47 MPa) owing to the dense multi-arch structure and tightly contacted graphene interfaces.[28] Nevertheless, surface treatment should be taken into account to make rGO materials zincophilic for stable Zn deposition.[10,29] Generally speaking, metallic species (such as Ag,[11,29] Cu,[16,18,30,31] and Sn[13,32]) can be incorporated to carbon hosts to reduce interfacial energy and depress HER at the surface of ZMAs. However, it is still at the infancy stage to exploit zincophilic 3D hosts with high mechanical properties for stable ZMAs under dwell-fatigue and high-pressure conditions.

Inspired by above considerations, we herein design Ag decorated rGO foam (denoted as AGF) as a 3D host for ZMA under dwell-fatigue condition. An interfacial self-assembling strategy using air bubbles template is employed to create 3D composite hydrogel with spontaneous reduction reactions for both rGO and Ag species. After consecutive freeze-thaw, wet-press, and air-drying treatments, AGF with multiple-arch structure is obtained. Of note, the dense structure and strong synergetic effect between rGO and Ag guarantee high compressive strength and superelasticity for AGF. Therefore, the robust AGF can effectively adapt the pressure-changing environment and provide sufficient space for Zn plating. Besides, Ag species can serve as zincophilic sites to induce the nucleation of Zn deposit at low overpotential. As expected, the AGF@Zn electrode demonstrates excellent cycling stability under normal and dwell-fatigue conditions.

2. Results and Discussion

Figure 1a illustrates the synthesis procedure of AGF by reduction to form a hydrogel, followed by freeze-thaw, wet-press, and air-drying processes. First, Tollens reagent, sodium dodecyl sulfate (SDS), and ascorbic acid (AA) are stirred vigorously to create dense bubbles in the GO solution (Figure S1, Supporting Information). Then, a follow-up hydrothermal reduction reaction changes GO and $[Ag(NH_3)_2]^+$ into Ag-rGO hydrogel with the assistance of AA. Then, gelation enables the formation of rGO with decorated Ag species around the micro-sized air bubbles as a 3D porous network (Figure 1b). During a sequential freeze-thaw treatment, ice crystals serve as reamers to pierce the Ag-rGO network into an open-cell configuration. After wet-pressing, internal air and water are squeezed out and Ag-rGO network is compressed in the axial direction to form compact channels. It should be mentioned that high robustness of Ag-rGO channels could maintain the overall layered configuration during the air-drying process for the final AGF (Figure 1c). Moreover, SDS serves as the foaming agent to keep the integrity of the porous structure for Ag-rGO during preparation and pressure tests (Figure S2, Supporting Information). Meanwhile, pure rGO foam (GF) host (Figure S3, Supporting Information) and planar Ag decorated rGO (AG) host (Figure S4, Supporting Information) are fabricated as control samples.

As confirmed by X-ray diffraction pattern, Ag (100), Ag (111), Ag (220), and Ag (311) peaks of metallic Ag (JCPDS No. 04–0783) can be observed in the AGF. As calculated from the thermogravimetric analysis, the weight ratio of Ag element in AGF is about 8.1% (Figure S5, Supporting Information). High-angle annular dark field-scanning transmission electron microscope (HAADF-STEM) image (Figure 1d) and the corresponding mapping results (Figure 1e) show the uniform distribution of C, N, O, and Ag elements in AGF without apparent agglomeration. X-ray photoelectron spectroscopy (XPS) is used to investigate the chemical composition of AGF. The peaks of C—O (286.3 eV), C═C (288.1 eV), and O—C═O (289.7 eV) of AGF shift to lower binding energy compared with those of GF (Figure S6a, Supporting Information).[33] Meanwhile, N doped GF ($NH_3{\cdot}H_2O$ solution treated GF, denoted as NG) shows even higher valence states for the carbonaceous species. These above results indicate the potential existence of Ag—N—G species in AGF. Two obvious peaks located at 368.4 and 374.4 eV can be observed in the Ag 3d XPS spectrum of AGF, corresponding to Ag $3d_{5/2}$ peak and Ag $3d_{3/2}$ peak (Figure S6b, Supporting Information). The spin separation energy (6.0 eV) indicates that Ag exists in both metallic and oxidation states within AGF.[34] The incorporation of Ag species induces the reduction of N species in AGF, which also confirms the interaction between Ag and N species (Figure S6c, Supporting Information). Raman spectra provide more information about the interaction between Ag and rGO (Figure S7, Supporting Information). Three prominent peaks in Raman data reflect the content of monolayer graphene with a single band electronic dispersion (2D peak, located at 2685 cm^{-1}),[35] sp^3-defect (D peak, located at 1350 cm^{-1}), and vacancy-like defect (D′ peak, located at 1620 cm^{-1}).[36,37] Meanwhile, the absence of D′ peak in AGF and the increase of I_D/I_G ratio from 1.29 for GF to 1.34 for AGF reveal that Ag species might locate in the vacancy defects of rGO to form sp^3 defects.[38] Besides, the enhancement of the 2D peak in AGF indicates the increase of sp^2 carbon.[35] Fourier transform infrared spectra (Figure S8, Supporting Information) further confirm the decrease of C—O group in AGF compared to GF, indicating the poor wettability of AGF and the improved stability of the Ag and rGO by the hybridization between the Ag and the sp^2 dangling bonds.[39] As shown in Figure 1f, AGF can bare a 1 kg loading and bounce back to the original height when the loading is removed, demonstrating its good elasticity. Moreover, the ultimate compressive strength of AGF is almost 150 MPa (Figure 1g), which is much better than that of GF and other reported aerogels (Table S1, Supporting Information).[24,27,28,40–43] Molecular dynamics simulations are performed to verify the reinforcement mechanism of Ag species. In Figure 1h, calculation models are shown. For AGF, the graphene could form a sandwich structure where the decorated Ag species (≈2% and is very close to the experimental value) are loosely distributed. And for GF, graphene is wrinkled with varying degrees (Figure S9, Supporting Information). With the increase of strain, the internal space is compressed, and the metallic Ag particles are firmly confined within the shrinking structure of AGF. The scenario for GF is different, where the compression leads to the gradual collapse of the wrinkling. It should be noticed that in the real situation, AGF possesses both of these two microscopic deformation mechanisms, while GF has only one of them. Before certain amount of strain (60% in experiment), the 3D rGO

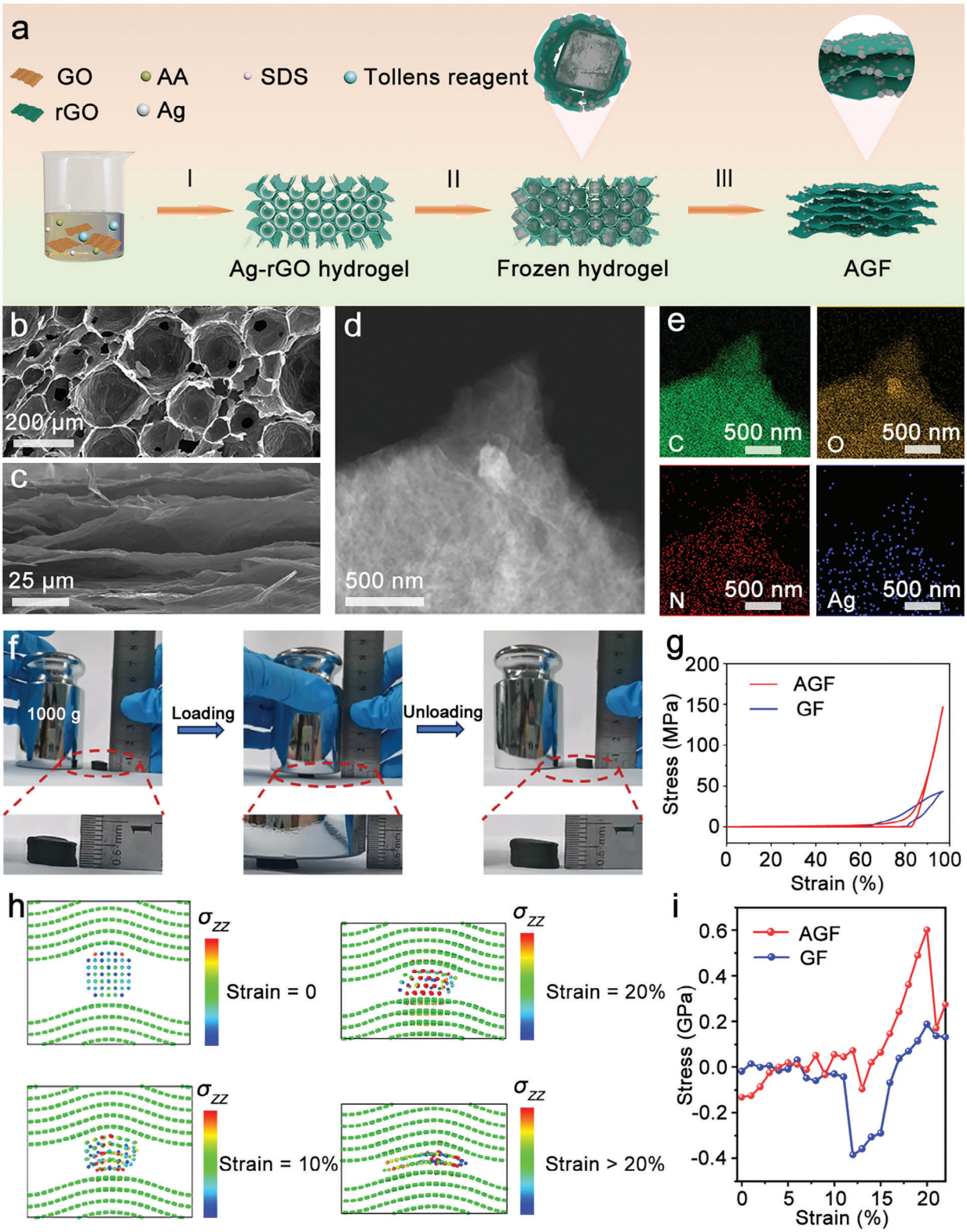

Figure 1. a) Schematic illustration of synthetic route for AGF. I) Reduction process. II) Frozen process. III) Wet-press process. Cross-sectional field-emission scanning electron microscope (FESEM) images of b) Ag-rGO hydrogel and c) AGF. d) HAADF-STEM image and e) the corresponding elemental mappings of AGF. f) Loading and unloading process of the AGF by a 1 kg weight. g) Compressive stress–strain curves of AGF and GF at 97% strain. h) Microscopic deformation mechanism of AGF, and colors represent the normal atomic stress along *z* direction (σ_{zz}). i) Corresponding strain and stress curves.

framework serves as the dominant role to withstand the stress at low strain values, and thus there is a negligible difference in stress–strain curves. However, further compression could trigger the pressure resistance of metallic Ag species, which greatly improve the compressive strength of AGF. The corresponding stress and strain curves are shown in Figure 1i, and it could be found that the predicted strength of AGF is comparable to the experimental measurements (150 MPa). One thing should be clarified that the stress drop of GF stems from the van der Waals attraction between graphene layers when touched, and could be barely observed in experiment since such a large proportion contact at atomic scale is nearly impossible from thermodynamic perspective.

Zn plating behavior on AGF is monitored by FESEM (Figure S10, Supporting Information). After plating of 2 mAh cm^{-2}, the AGF host shows slight morphological changes, indicating the epitaxial deposition of Zn along the basal plane of Ag-decorated rGO sheets. With the increase of plating capacity, subsequent Zn deposits still keep the original morphology. When the deposition capacity reaches to 12 mAh cm^{-2}, gaps between adjacent channels within AGF are almost filled with deposited Zn. Large-scale observations indicate the stable deposition without the formation of dendrite (Figure S11, Supporting Information). On the contrary, Zn plating on GF is out of control due to the zincophobic surface and flat surface and a large number of loosely stacked Zn dendrites can be identified on the entire surface of GF host (Figures S12 and S13 Supporting Information). As a control, Zn agglomeration can be found on the surface of AG at high deposition capacity, although the incorporation of Ag particles can facilitate the Zn plating (Figure S14, Supporting Information). Moreover, the decoration of Ag species also facilitates the reversible stripping of Zn and no inactive Zn residual can be seen (Figure S15, Supporting Information).

Density functional theory (DFT) calculations are carried out to gain insights into the function of individual component of AGF during Zn deposition (**Figure 2**a). Figure 2b shows the calculated binding energies (E_b) between Zn atom and various components in the AGF host. It is noteworthy that Ag (100) exhibits the highest E_b, indicating the strong Zn affinity of Ag species. Compared to graphene (G), Ag/N-doped graphene (Ag—N—G) also shows enhanced interaction with Zn. Moreover, the DFT-based interfacial charge density models reveal Ag (100) could provide the strongest affiliation with Zn (Figure 2c). Generally, high zincophilicity could reduce the nucleation energy barrier for uniform deposition. As expected, AGF with zincophilic Ag species shows the lowest nucleation overpotential about 16 mV among samples in half cells (Figure 2d and Figure S16, Supporting Information). Figure 2e shows that the AGF host presents superior performance over GF with a high average Coulombic efficiency (CE) of 99.5% over 1000 cycles at 5 mA cm^{-2} for 1 mAh cm^{-2}. Ag species are firmly anchored on AGF to prevent the potential dissolution into the electrolyte during cycling (Figure S17 and Table S2, Supporting Information). Moreover, AGF also presents much better CE values than GF and AG at a high current density of 10 mA cm^{-2} (Figure S18, Supporting Information). Cyclic voltammetry (CV) curves also demonstrate the superiority of AGF over GF, which could facilitate the Zn deposition at lower overpotential (Figure 2f). Furthermore, the initial three CV cycles of AGF overlap well, suggesting good reversibility (Figure S19, Supporting Information). In addition, the AGF host displays zincophilic nature, which shows inferior HER performance over GF (Figure 2g).

Figure 3a shows in situ Zn plating behaviors for the AGF@Zn electrode, which presents a smooth and uniform deposition at a high current density of 10 mA cm^{-2}. In contrast, small protrusions and uneven Zn deposits appear at the edge of Zn foil after only 10 min and develop into rampant dendrites (Figure 3b). Symmetric cells using AGF hosts or control samples with pre-electroplated Zn are assembled to appraise the long-term cycling performance. Figure 3c illustrates that AGF@Zn presents the longest cycling over 1600 h at 3 mA cm^{-2} with the smallest voltage hysteresis about 30 mV among different electrodes (Figure S20, Supporting Information). Of note, AGF@Zn electrode shows a neat surface without Zn dendrites after 50 cycles. As reference, uneven depositions with massive Zn dendrites are observed on Zn foil and GF@Zn electrodes (Figure S21, Supporting Information). Moreover, the symmetric cell using the AGF@Zn electrodes can still operate steadily over 1400 h at a higher current density of 10 mA cm^{-2} (Figure 3d). In contrast, the stable lifespan for symmetric cell using GF@Zn electrodes is only 250 h (Figure S22, Supporting Information). Even at a high depth-of-discharge (DOD) of 50% and high current density of 10 mA cm^{-2}, the AGF@Zn based symmetric cell can still function well over 400 h (Figure S23, Supporting Information). Compared with previous reported hosts operating at high DOD values, the electrochemical performance of AGF@Zn electrode is also remarkable (Table S3, Supporting Information).[9,12,18,29,44,45] Moreover, Figure 3e demonstrates that the AGF@Zn electrode exhibits better rate performance than Zn foil and GF@Zn electrode (Figure S24, Supporting Information). The excellent electrochemical performances of AGF@Zn are comparable to those of other composite Zn electrodes in symmetric cells (Figure 3f and Table S4, Supporting Information).[9,13,21,22,29,44,46–48] Moreover, electrochemical impedance tests at various temperatures and the corresponding Arrhenius activation energy (E_a) data show the AGF@Zn electrode has faster kinetics of Zn deposition than the control samples (Figure S25, Supporting Information).

To simulate the working condition at deep ocean, a polyether ether ketone (PEEK) mold with stainless steel plungers (**Figure 4**a) is used for the cell assembly and evaluated under different stack pressures.[3,4] As shown in Figure 4b, Zn plating behaviors on the AGF host under different pressures are similar to those under the normal condition in coin cell. The nucleation overpotentials under varying pressures are almost the same. But we should point out that the ion migration at the interface for AGF is affected at high pressure, which might influence the long-term performance. The AGF host can survive even the applied load is as high as 88 MPa, showing the high mechanical strength. However, the separator experiences severe and fast pulverization under high pressure, which may cause the rapid short circuit (Figure S26, Supporting Information). Besides, high CE values and steadily voltage profiles indicate that the Zn plating and stripping processes under high pressures on AGF are analogous to the normal conditions (Figure 4c,d). However, the durability of AGF is indeed changed and cycling performances in the symmetric cells using AGF@Zn electrode under high pressures are quite different from those in coin cell (Figure 4e).

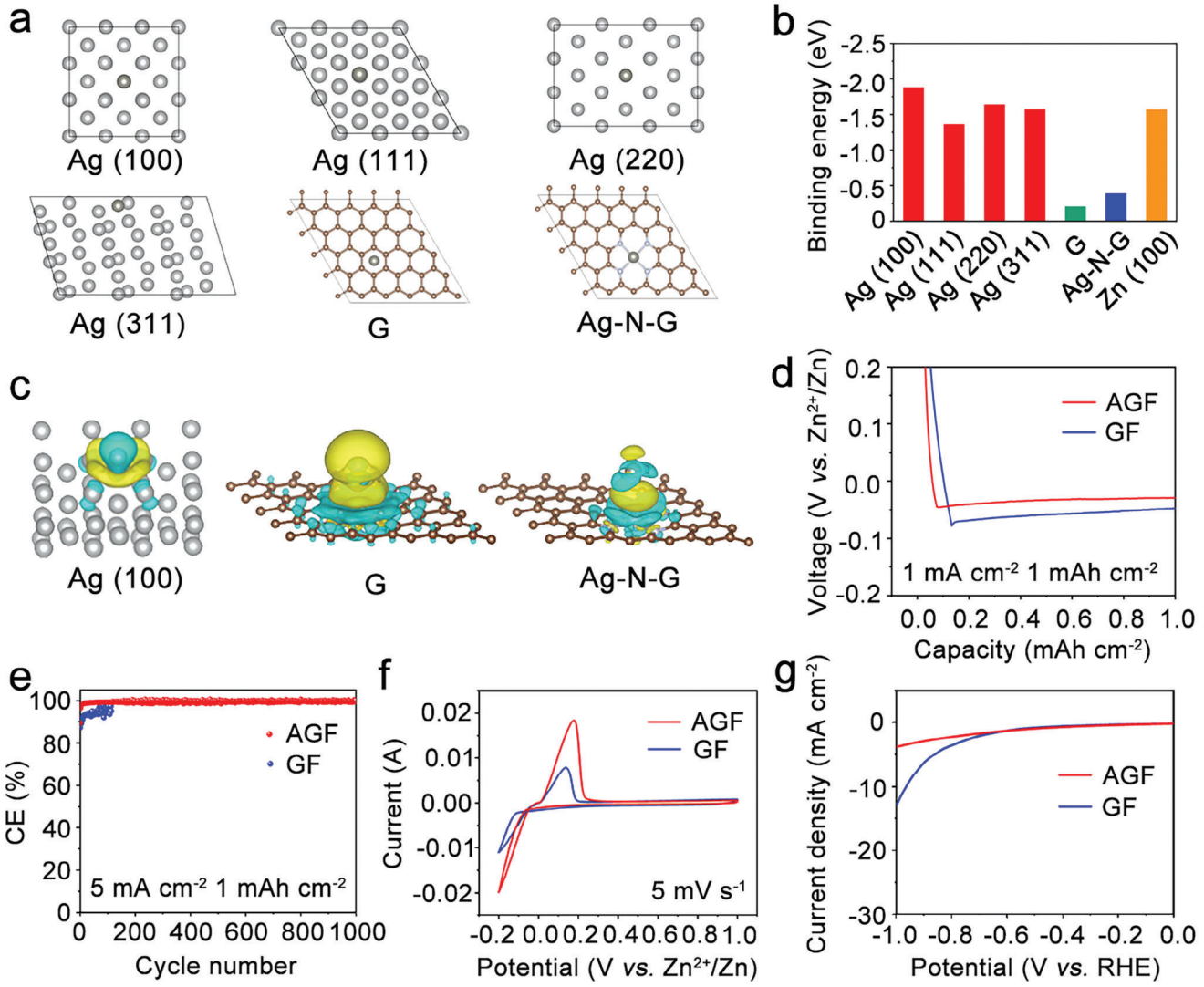

Figure 2. a) DFT calculation models of Ag (100), Ag (111), Ag (220), Ag (311), G, and Ag—N—G. b) Summary of the calculated E_b of Zn atom with Ag (100), Ag (111), Ag (220), Ag (311), G, and Ag—N—G in DFT, and Zn (100). c) Interfacial charge-density models of Ag (100), G, and Ag—N—G. d) Voltage profiles, e) CE plots, f) CV curves, and g) HER performance of AGF and GF.

Although the AGF@Zn electrode demonstrates a long cycle life over 120 h under 26 MPa, the lifespan is sharply shortened with the increase of the external load. Of note, the AGF@Zn can still function well under the stack pressure of 88 MPa, even at a high DOD of 50% (Figure S27, Supporting Information). On the contrary, the symmetric cell using Zn foil shows a quick capacity decay under the pressure of 88 MPa (Figure S28, Supporting Information). More importantly, symmetric cell using AGF@Zn still survives under the dwell-fatigue condition. Starting from the external load of 8.8 MPa, the AGF@Zn electrode can maintain a stable cycling during the continuous unloading processes to 0.44 MPa (Figure 4f). Whereas, symmetric cell using Zn foil experiences drastic voltage fluctuations after unloading to 0.88 MPa and a sudden cell failure after unloading to 0.44 MPa (Figure 4g). It can be deduced that the superelastic AGF can restore to the original state after the unloading process to keep contact between the electrode and the separator.

To further verify the feasibility of this AGF host in practical applications, full cell using ammonium vanadate ($NH_4V_4O_{10}$, denoted as NVO) cathode (Figure S29, Supporting Information) and AGF@Zn or Zn foil anode is assembled. Compared with Zn||NVO full cell, AGF@Zn||NVO full cell presents a smaller voltage difference between two redox peaks in the CV curve (**Figure 5a**), further confirming the promoted ion transfer. Moreover, AGF@Zn||NVO delivers average capacities of 457, 391, 340, 262, and 143 mAh g^{-1} at the current densities of 1, 2, 3, 5, and 10 A g^{-1}, respectively (Figure 5b). Besides, AGF@Zn||NVO presents better rate capabilities and long-term capacity retention over 3000 cycles than Zn||NVO (Figure 5c,d). It is worth noting that the AGF@Zn||NVO cell suffers from activation processes during the initial cycles, which might be attributed to the hydrophobicity of the AGF (Figure S30, Supporting Information). Moreover, two pouch cells using AGF@Zn||NVO can light up a light-emitting diode (LED) screen with a shape of "BUCT" under

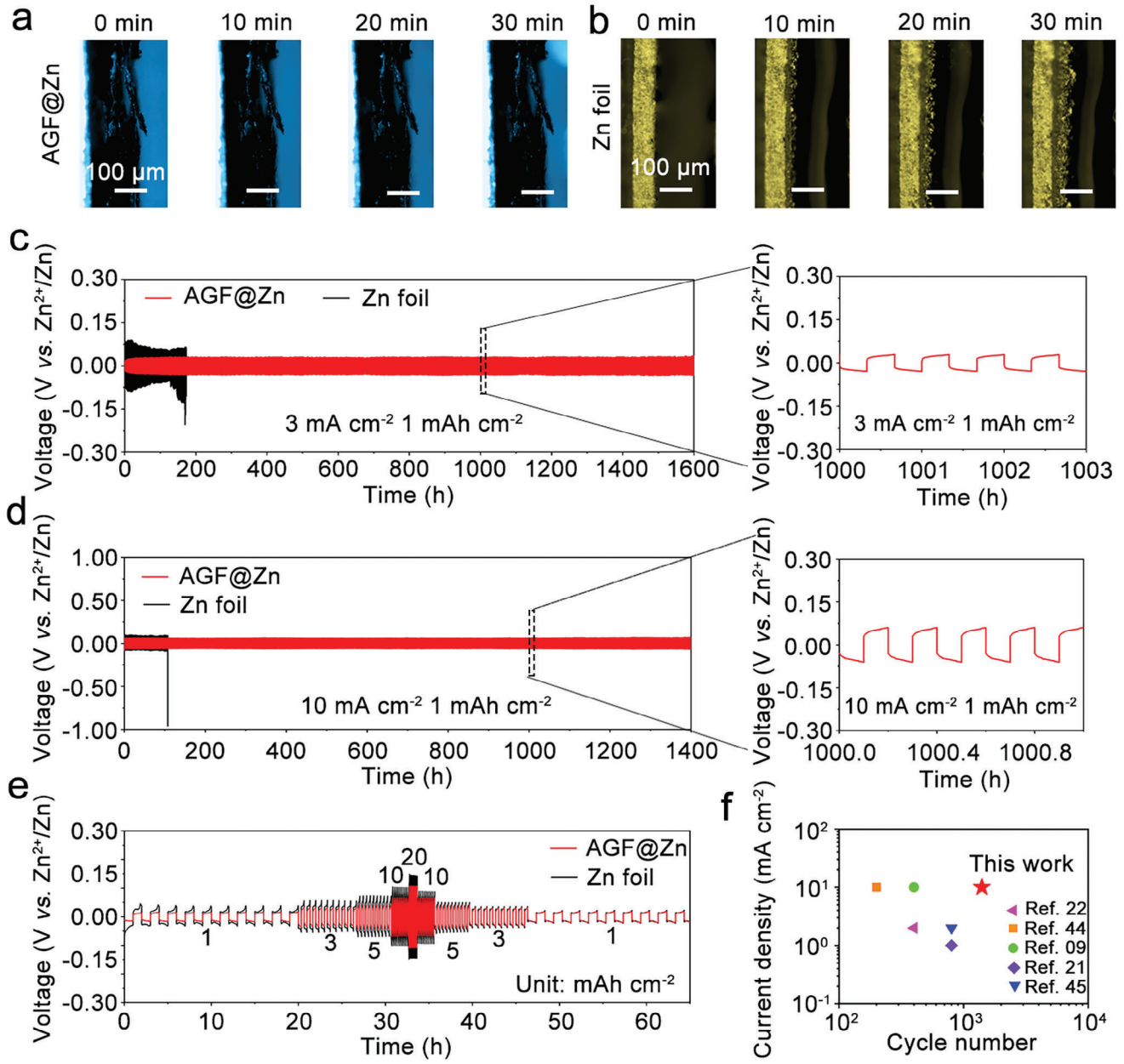

Figure 3. In situ optical observations of Zn plating on a) AGF and b) Zn foil at 10 mA cm^{-2}. Cycling performance of symmetric cells at c) 3 mA cm^{-2} for 1 mAh cm^{-2} and d) 10 mA cm^{-2} for 1 mAh cm^{-2}. e) Rate performance of different symmetric cells. f) Comparison of symmetric cells using different hosts.

various bending states (0°, 45°, 90°, 180°) (Figure S31, Supporting Information), demonstrating the potential application value. Even tested under high stack pressure (26 MPa) in PEEK mold, the AGF@Zn||NVO full cell also demonstrates longer lifespan than the control cell (Figure S32, Supporting Information). More importantly, we carry out a deep-sea environmental pressure simulation test using pouch cells. After the continuous pressure loading and unloading processes, the AGF@Zn||NVO pouch cells can still function well to power a LED device (Figure S33, Supporting Information).

3. Conclusions

In summary, we report the synthesis of robust AGF as a Zn host for ZMAs in extreme environment by a multi-step assembly strategy. The dense configuration and strong synergetic effect between rGO and Ag promote the elasticity and mechanical strength for AGF. Meanwhile, the porous framework with the decorated Ag species has the potential for the preferential Zn deposition in the confined space. As expected, the AGF host realizes steady Zn plating/stripping at high current density and DOD in

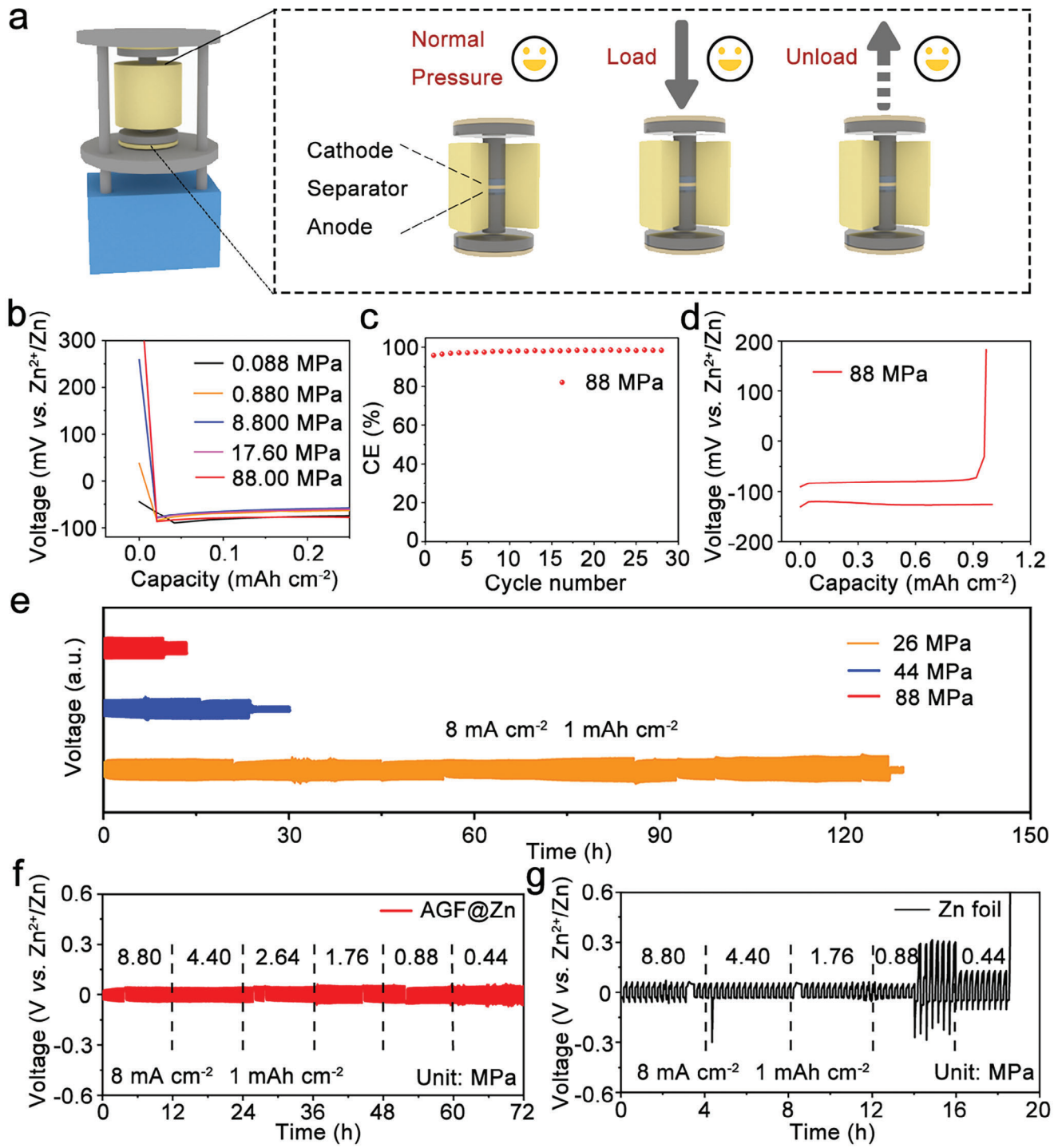

Figure 4. a) Device illustration for pressure control during cycling. b) Voltage profiles of Zn plating on AGF in half cell under different stacking pressures at 5 mA cm^{-2}. c) CE plot, and d) plating/stripping profiles at 5 mA cm^{-2} for 1 mAh cm^{-2} for AGF under 88 MPa in half cells. e) Voltage profiles of AGF@Zn symmetric cell as a function of time at different stack pressures. Cycling performance with continuous unloading process for symmetric cells using f) AGF@Zn and g) Zn foil.

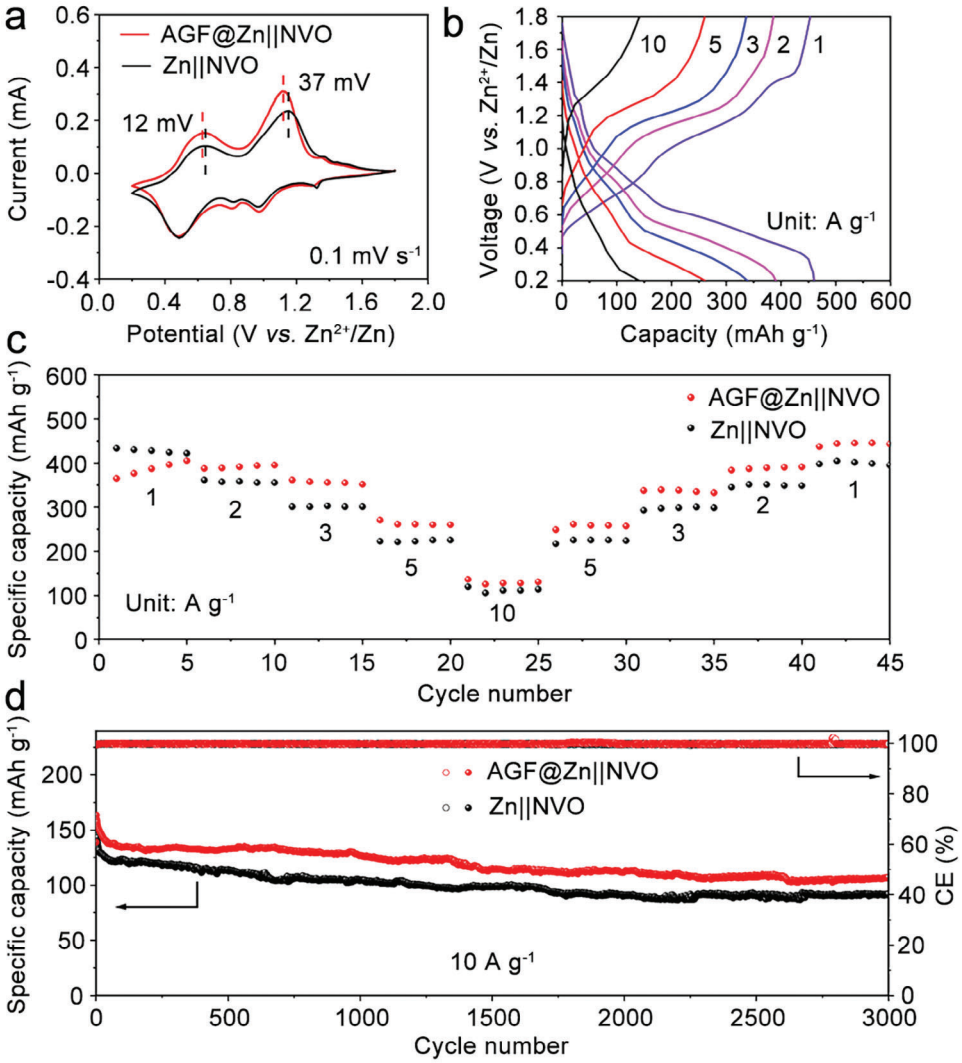

Figure 5. a) CV curves of AGF@Zn||NVO and Zn||NVO. b) Charge/discharge profiles of AGF@Zn||NVO at different current densities. c) Rate capability, and d) cycling performances of AGF@Zn||NVO and Zn||NVO.

the coin cell. More importantly, the robustness of the AGF host guarantees its high performance under varying pressures and dwell-fatigue condition.

Supporting Information

Supporting Information is available from the Wiley Online Library or from the author.

Acknowledgements

This work was supported by the National Natural Science Foundation of China (Grant Nos. U22A20145 and 22278019), the Natural Science Foundation of Beijing (L223008), the Foundation of State Key Laboratory of Organic-Inorganic Composites (oic-202301013), and the Double Thousand Plan of Jiangxi Province (S2021DQKJ1886).

Conflict of Interest

The authors declare no conflict of interest.

Data Availability Statement

The data that support the findings of this study are available from the corresponding author upon reasonable request.

Keywords

Ag, dwell fatigue, reduced graphene oxide, superelastic, Zn metal anode

Received: April 25, 2024
Revised: June 15, 2024
Published online: June 29, 2024

[1] C. J. Niu, H. L. Pan, W. Xu, J. Xiao, J. G. Zhang, L. L. Luo, C. M. Wang, D. H. Mei, J. S. Meng, X. P. Wang, Z. Liu, L. Q. Mai, J. Liu, *Nat. Nanotechnol.* **2019**, *14*, 594.
[2] J. L. Wu, Y. L. Wu, L. G. Wang, H. L. Ye, J. Lu, Y. G. Li, *Adv. Mater.* **2023**, *36*, 2308193.

[3] H. F. Xu, Q. Zhu, Y. Zhao, Z. G. Du, B. Li, S. B. Yang, *Adv. Mater.* **2023**, *35*, 2212111.
[4] J. M. Doux, H. Nguyen, D. H. S. Tan, A. Banerjee, X. F. Wang, E. A. Wu, C. Jo, H. D. Yang, Y. S. Meng, *Adv. Energy Mater.* **2020**, *10*, 1903253.
[5] M. Z. Chen, Y. Y. Zhang, G. C. A. Xing, S. L. Chou, Y. X. Tang, *Energy Environ. Sci.* **2021**, *14*, 3323.
[6] Z. L. Zhang, G. D. Chen, Y. Xue, Q. F. Duan, X. Y. Liang, T. Lin, Z. X. Wu, Y. Tan, Q. Zhao, W. Q. Zheng, L. A. Wang, F. C. Wang, X. Y. Luo, J. K. Xu, J. Liu, B. Y. Lu, *Adv. Funct. Mater.* **2023**, *33*, 2305705.
[7] S. J. Wu, H. J. Li, D. N. Futaba, G. H. Chen, C. Chen, K. C. Zhou, Q. F. Zhang, M. Li, Z. L. Ye, M. Xu, *Adv. Mater.* **2022**, *34*, 2201046.
[8] C. W. Zheng, S. Y. Zhou, Z. Q. Chen, Y. L. Ge, D. Y. Huang, J. Liu, Q. Yang, *J Zhejiang Univ Sci* **2018**, *19*, 774.
[9] P. Xue, C. Guo, L. Li, H. P. Li, D. Luo, L. C. Tan, Z. W. Chen, *Adv. Mater.* **2022**, *34*, 2110047.
[10] Y. B. Mu, Z. Li, B. K. Wu, H. D. Huang, F. H. Wu, Y. Q. Chu, L. F. Zou, M. Yang, J. F. He, L. Ye, M. S. Han, T. S. Zhao, L. Zeng, *Nat. Commun.* **2023**, *14*, 4205.
[11] J. X. Zheng, Y. C. Wu, H. X. Xie, Y. Zeng, W. Q. Liu, A. N. Gandi, Z. C. Wang, Z. B. Qi, H. F. Liang, *ACS Nano* **2023**, *17*, 337.
[12] J. B. Park, C. Choi, J. H. Park, S. Yu, D. W. Kim, *Adv. Energy Mater.* **2022**, *12*, 2202937.
[13] H. Yu, Y. X. Zeng, N. W. Li, D. Y. Luan, L. Yu, X. W. Lou, *Sci. Adv.* **2022**, *8*, eabm5766.
[14] X. H. Chen, P. C. Ruan, X. W. Wu, S. Q. Liang, J. Zhou, *Acta Phys. Chim. Sin.* **2022**, *38*, 2111003.
[15] M. Song, C. L. Zhong, *Rare Met.* **2022**, *41*, 356.
[16] Y. Z. Li, Q. Z. Zhu, M. Y. Xu, B. Y. Zang, Y. Wang, B. Xu, *Adv. Funct. Mater.* **2023**, *33*, 2213416.
[17] G. P. Li, X. L. Wang, S. H. Lv, J. X. Wang, W. S. Yu, X. T. Dong, D. T. Liu, *Adv. Funct. Mater.* **2023**, *33*, 2208288.
[18] Y. X. Zeng, Z. H. Pei, D. Y. Luan, X. W. Lou, *J. Am. Chem. Soc.* **2023**, *145*, 12333.
[19] X. F. Shen, X. N. Wang, N. S. Yu, W. Yang, Y. R. Zhou, Y. H. Shi, Y. L. Wang, L. Z. Dong, J. T. Di, Q. W. Li, *Acta Phys. Chim. Sin.* **2022**, *38*, 2006059.
[20] C. X. Xu, J. J. Jiang, *Rare Met.* **2021**, *40*, 749.
[21] Y. Yang, C. Y. Liu, Z. H. Lv, H. Yang, Y. F. Zhang, M. H. Ye, L. B. Chen, J. B. Zhao, C. C. Li, *Adv. Mater.* **2021**, *33*, 2007388.
[22] Y. X. Zeng, P. X. Sun, Z. H. Pei, Q. Jin, X. T. Zhang, L. Yu, X. W. Lou, *Adv. Mater.* **2022**, *34*, 2200342.
[23] S. N. Yang, H. X. Du, Y. T. Li, X. S. Wu, B. S. Xiao, Z. X. He, Q. B. Zhang, X. W. Wu, *Green Energy Environ.* **2023**, *8*, 1531.
[24] H. L. Guo, Q. Y. Fei, M. Lian, T. Y. Zhu, W. Fan, Y. M. Li, L. Sun, F. de Jong, K. B. Chu, W. Zong, C. Zhang, T. X. Liu, *Adv. Mater.* **2023**, *35*, 202301418.
[25] H. L. Jin, Y. F. Bu, J. Li, J. P. Liu, X. Fen, L. M. Dai, J. C. Wang, J. Lu, S. Wang, *Adv. Mater.* **2018**, *30*, 1707424.
[26] D. M. Tang, C. L. Ren, L. Zhang, Y. Tao, P. Zhang, W. Lv, X. L. Jia, X. J. Jiang, G. M. Zhou, T. Ohmura, P. Huai, F. Li, Y. Bando, D. Golberg, Q. H. Yang, *Adv. Funct. Mater.* **2019**, *29*, 1900311.
[27] L. Zhuang, D. Lu, J. J. Zhang, P. F. Guo, L. Su, Y. B. Qin, P. Zhang, L. Xu, M. Niu, K. Peng, H. J. Wang, *Nat. Commun.* **2023**, *14*, 3178.
[28] H. S. Yang, Z. L. Li, G. Q. Sun, X. T. Jin, B. Lu, P. P. Zhang, T. Y. Lin, L. T. Qu, *Adv. Funct. Mater.* **2019**, *29*, 1901917.
[29] T. Chen, Y. A. Wang, Y. Yang, F. Huang, M. K. Zhu, B. T. W. Ang, J. M. Xue, *Adv. Funct. Mater.* **2021**, *31*, 2101607.
[30] L. J. Zhou, F. Yang, S. Q. Zeng, X. Y. Gao, X. Q. Liu, X. S. Cao, P. Yu, X. H. Lu, *Adv. Funct. Mater.* **2022**, *32*, 2110829.
[31] W. Y. Zhang, Q. S. Yao, C. Wang, R. F. Feng, N. Chen, J. W. Zhu, Z. Li, *Adv. Funct. Mater.* **2023**, *34*, 2303590.
[32] Q. Y. Jiao, X. W. Zhai, Z. X. Sun, W. J. Wang, S. H. Liu, H. Ding, W. S. Chu, M. Zhou, C. Z. Wu, *Adv. Mater.* **2023**, *35*, 2300850.
[33] H. J. Huang, D. S. Yu, F. Hu, S. C. Huang, J. N. Song, H. Y. Chen, L. L. Li, S. J. Peng, *Angew. Chem., Int. Ed.* **2022**, *61*, e202116068.
[34] Z. L. Tang, W. J. He, Y. L. Wang, Y. C. Wei, X. L. Yu, J. Xiong, X. Wang, X. Zhang, Z. Zhao, J. Liu, *Appl. Catal., B* **2022**, *311*, 121371.
[35] X. Li, W. C. H. Choy, X. Ren, D. Zhang, H. Lu, *Adv. Funct. Mater.* **2014**, *24*, 3114.
[36] A. Zandiatashbar, G. H. Lee, S. J. An, S. Lee, N. Mathew, M. Terrones, T. Hayashi, C. R. Picu, J. Hone, N. Koratkar, *Nat. Commun.* **2014**, *5*, 3186.
[37] A. Eckmann, A. Felten, A. Mishchenko, L. Britnell, R. Krupke, K. S. Novoselov, C. Casiraghi, *Nano Lett.* **2012**, *12*, 3925.
[38] P. Huang, Z. Cheng, L. Zeng, L. L. Tan, J. Yu, J. Rushikesh, L. S. Fan, Y. J. Zhu, *J. Mater. Chem. A* **2022**, *10*, 8245.
[39] S. Chen, X. Hai, X. W. Chen, J. H. Wang, *Anal. Chem.* **2014**, *86*, 6689.
[40] J. Y. Zhu, Y. L. Zhu, Y. H. Ye, Z. Qiu, Y. F. Zhang, Z. Y. Yu, X. Sun, D. C. Bressler, F. Jiang, *Adv. Funct. Mater.* **2023**, *33*, 2300893.
[41] D. D. Zong, W. Y. Bai, X. Yin, J. Y. Yu, S. C. Zhang, B. Ding, *Adv. Funct. Mater.* **2023**, *33*, 2301870.
[42] X. Chang, F. Wu, X. Cheng, H. Zhang, L. He, W. Li, X. Yin, J. Yu, Y. T. Liu, B. Ding, *Adv. Mater.* **2023**, *36*, 2308519.
[43] S. A. Hashemi, A. Ghaffarkhah, M. Goodarzi, A. Nazemi, G. Banvillet, A. S. Milani, M. Soroush, O. J. Rojas, S. Ramakrishna, S. Wuttke, T. P. Russell, M. Kamkar, M. Arjmand, *Adv. Mater.* **2023**, *35*, 2302826.
[44] P. X. Sun, Z. J. Cao, Y. X. Zeng, W. W. Xie, N. W. Li, D. Y. Luan, S. B. Yang, L. Yu, X. W. Lou, *Angew. Chem., Int. Ed.* **2022**, *61*, e202115649.
[45] H. Yu, H. X. Yao, Y. Q. Zheng, D. Liu, J. S. Chen, Y. Guo, N. W. Li, L. Yu, *Adv. Funct. Mater.* **2023**, *34*, 2311038.
[46] J. H. Zhou, F. Wu, Y. Mei, Y. T. Hao, L. Li, M. Xie, R. J. Chen, *Adv. Mater.* **2022**, *34*, 2200782.
[47] X. Li, M. Li, K. Luo, Y. Hou, P. Li, Q. Yang, Z. Huang, G. Liang, Z. Chen, S. Du, Q. Huang, C. Zhi, *ACS Nano* **2021**, *16*, 813.
[48] J. H. Zhou, M. Xie, F. Wu, Y. Mei, Y. T. Hao, L. Li, R. J. Chen, *Adv. Mater.* **2022**, *34*, 2106897.